Differential clock comparisons with a multiplexed optical lattice clock

https://doi.org/10.1038/s41586-021-04344-y

Received: 24 September 2021

Accepted: 14 December 2021

Published online: 16 February 2022



Check for updates

Xin Zheng¹, Jonathan Dolde¹, Varun Lochab¹, Brett N. Merriman¹, Haoran Li¹ & Shimon Kolkowitz^{1⊠}

Rapid progress in optical atomic clock performance has advanced the frontiers of timekeeping, metrology and quantum science¹⁻³. Despite considerable efforts, the instabilities of most optical clocks remain limited by the local oscillator rather than the atoms themselves^{4,5}. Here we implement a 'multiplexed' one-dimensional optical lattice clock, in which spatially resolved strontium atom ensembles are trapped in the same optical lattice, interrogated simultaneously by a shared clock laser and read-out in parallel. In synchronous Ramsey interrogations of ensemble pairs we observe atom-atom coherence times of 26 s, a 270-fold improvement over the measured atom-laser coherence time, demonstrate a relative instability of $9.7(4) \times 10^{-18} / \sqrt{\tau}$ (where τ is the averaging time) and reach a relative statistical uncertainty of 8.9×10^{-20} after 3.3 h of averaging. These results demonstrate that applications involving optical clock comparisons need not be limited by the instability of the local oscillator. We further realize a miniaturized clock network consisting of 6 atomic ensembles and 15 simultaneous pairwise comparisons with relative instabilities below $3 \times 10^{-17} / \sqrt{\tau}$, and prepare spatially resolved, heterogeneous ensemble pairs of all four stable strontium isotopes. These results pave the way for multiplexed precision isotope shift measurements, spatially resolved characterization of limiting clock systematics, the development of clock-based gravitational wave and dark matter detectors⁶⁻¹² and new tests of relativity in the lab¹³⁻¹⁶.

Neutral atom optical lattice clocks (OLCs) have recently reached instability and inaccuracy at the 10⁻¹⁸ level^{2-5,17-21} largely due to the narrow linewidths of optical frequency forbidden clock transitions in alkaline-earth(-like) atoms. This performance enables new clock applications such as in relativistic geodesy, searches for dark matter, gravitational wave detection and tests of fundamental physics $^{6-16}$.

Many emerging clock applications rely on differential comparisons between two or more optical clocks, rather than on the determination of the absolute frequencies of the clock transitions. For atoms in unentangled states, the instability of such clock comparisons is fundamentally limited by quantum projection noise (QPN)²². For Ramsey spectroscopy, the QPN limit for the fractional frequency uncertainty of a clock comparison is given by

$$\sigma_{\rm QPN}(\tau) = \frac{\sqrt{2}}{2\pi\nu CT} \sqrt{\frac{T + T_{\rm d}}{N\tau}},$$
 (1)

where v is the transition frequency, T is the interrogation time, T_d is the dead time between experiment cycles, τ is the averaging time, N is the atom number per clock per measurement, C is the contrast of Ramsey fringes and the factor of $\sqrt{2}$ assumes an equal contribution from each clock. Equation (1) implies that the instability can be reduced with greater atom numbers and longer coherence times. However, frequency noise in the clock lasers used to interrogate the atoms limits the atom-laser coherence times, and also prevents the clock instability from reaching the QPN limit for larger atom numbers due to the Dick effect^{18,23}, which is an aliasing of frequency noise due to non-continuous laser interrogation. This motivates the use of synchronous differential comparisons^{4,24}, also known as correlated noise spectroscopy²⁵, for applications involving clock comparisons^{7,14}. Common-mode rejection of Dick noise and 10-s-scale atom-atom coherence times have recently been demonstrated between two independent ion clocks²⁶, between subensembles in a three-dimensional Fermi-degenerate OLC^{2,19} and between subensembles in a tweezer-array clock²⁷. In each of these cases the atoms are individually and tightly confined, suggesting that strong confinement and a lack of atom-atom interactions may be necessary ingredients to achieve such long coherent interrogation times. Furthermore, the best relative instabilities observed thus far, in the range of $3 \times 10^{-17}/\sqrt{\tau}$ (refs. ^{2,19,27}), have made use of an 8 mHz linewidth clock laser with an instability of 4×10^{-17} at 1 s (ref. ²⁸), suggesting that, even in synchronous differential comparisons, clock laser coherence could still play a role in limiting the achievable instability.

Here we introduce and implement an alternative platform for differential clock comparisons with a spatially 'multiplexed' OLC in a vertical, shallow one-dimensional (1D) lattice. Synchronous differential comparisons between spatially separated ensembles reject common-mode noise, including local oscillator noise and environmental systematic effects such as black-body radiation (BBR) and a.c. Stark

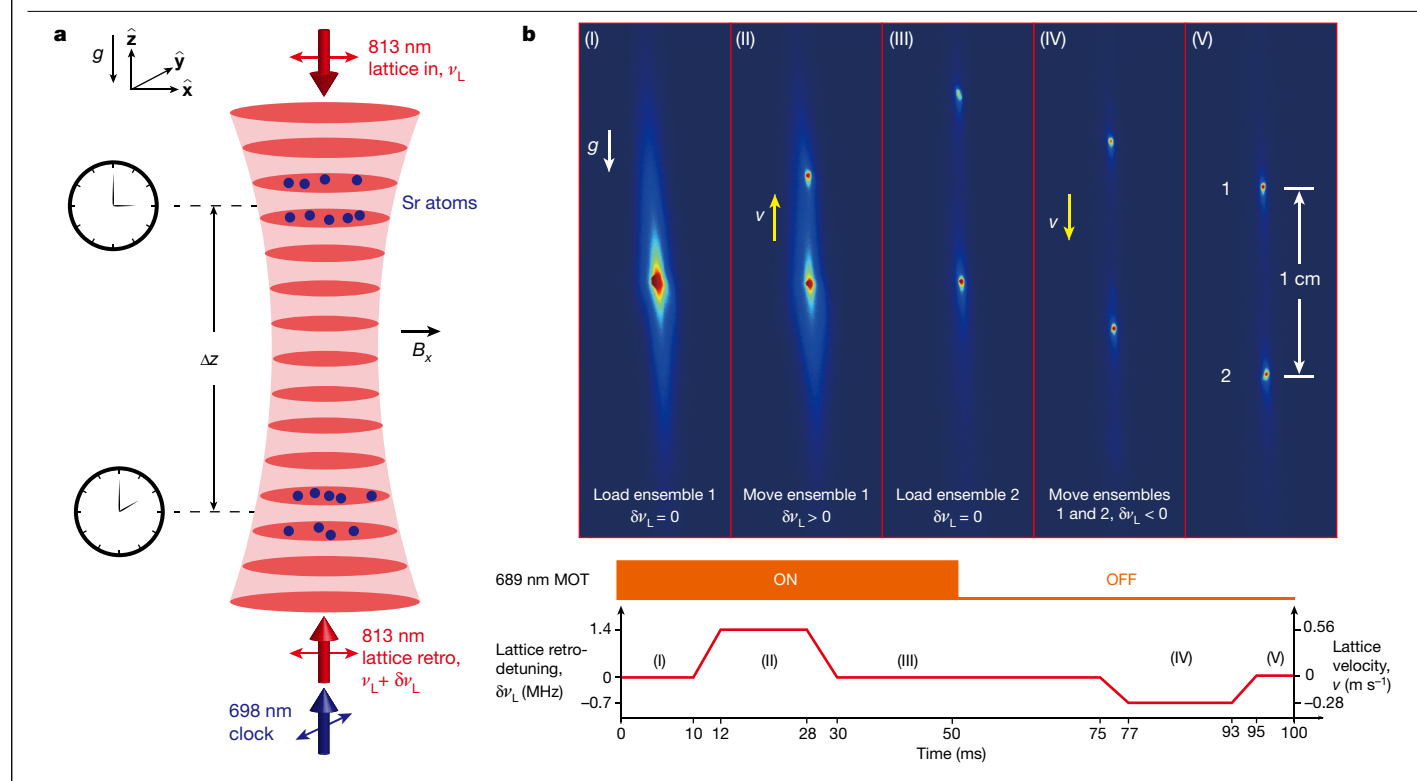


Fig. 1| **Multiplexed OLC configuration and procedure for loading two ensembles. a**, Schematic diagram illustrating the multiplexed OLC concept. Two ensembles of strontium atoms separated by Δz in height are prepared for synchronous clock interrogation using a shared clock laser. A movable lattice is formed by detuning the lattice retro-frequency $(v_L + \delta v_L)$ from the incoming lattice frequency (v_L) (see Methods for details). A bias magnetic field $(B_x$, about 2 G) in the $\hat{\mathbf{x}}$ direction defines the quantization axis. **b**, Top, camera images

taken during loading stages (I)–(V). (I) Loading ensemble 1 into the lattice; (II) separating ensemble 1 from the original atomic cloud by accelerating the lattice along $+\hat{z}$; (III) loading ensemble 2 into the lattice; (IV) simultaneously moving both ensembles along $-\hat{z}$; (V) two stationary ensembles with a height difference of 1 cm are prepared for spin-polarization, in-lattice cooling and clock interrogation. Bottom, timing sequence diagram for the 689 nm MOT and lattice retro-detuning, corresponding to the camera images shown above.

shifts from the lattice. As a result, we demonstrate atom–atom coherence times of 26 s, clock comparisons with relative instability below $10^{-17}/\sqrt{\tau}$ and a relative statistical uncertainty below the 10^{-19} level.

Our results demonstrate that decoherence due to atomic collisions 2,29,30 , and 2,29,30 coupling of motion between the axial and radial modes³¹ and tunneling³² do not yet limit the perfomance of 1D OLCs, and show that differential clock comparisons enable good relative instability without requiring state-of-the-art millihertz-linewidth clock lasers. This has important implications for applications that require portable or space-based clocks. such as relativistic geodesy and gravitational wave detection^{7,14}. We show that the same approach scales to the multiplexing of larger numbers of clock ensembles, with relative instabilities on a par with state-of-the-art clock comparisons, and can be used to load heterogeneous spatially resolved pairs of all four stable isotopes of strontium in the same lattice. The multiplexed OLC therefore represents a new platform that can test the limits of achievable instability in differential clock comparisons, including those with entangled atomic states33, while enabling new tabletop tests of relativity^{13,16}, precision searches for new physics beyond the Standard Model⁶, development and testing of new protocols for clock-network-based dark matter and gravitational wave detectors⁷⁻¹¹, and spatially resolved characterization of limiting clock systematics³⁴.

The basic concept of the 'multiplexed' OLC is illustrated in Fig. 1a, in which a movable 1D optical lattice is used to deterministically prepare multiple spatially resolved ensembles. The experimental procedure for preparing two ensembles separated by 1 cm in the \hat{z} direction is shown in Fig. 1b, where five representative images are shown for loading and moving the lattice such that two ensembles with a tuneable separation centred about the lattice beam waist are prepared. In our apparatus, a few thousand atoms can be loaded in each ensemble with spatial separations ranging from lower than 1 mm to more than 1 cm in under 100 ms.

We interrogate the ${}^1S_0 \leftrightarrow {}^3P_0$ clock transition with a 698 nm clock laser that is referenced to a rack-mounted ultra-low-expansion (ULE) cavity. Limited by this cavity, we expect an instantaneous local oscillator linewidth of approximately 1 Hz and a linear drift rate of approximately 1 Hz s⁻¹ before drift cancellation. This is orders of magnitude worse than state-of-the-art cavities such as cryogenic ultra-stable silicon cavities 28,35 , with measured linewidths of 8 mHz and linear drift rates smaller than 1 mHz s⁻¹ (ref. 36), which have been used to demonstrate relative instabilities at the low 10^{-19} level 2,19,27 .

To characterize the limitations placed on the coherent interrogation time by the clock laser linewidth, we first study each ensemble independently. A representative Rabi spectrum with a 10 Hz linewidth is shown in Fig. 2a, in which a π pulse of 90 ms duration is used to drive the $|{}^{1}S_{0}, m_{F} = 9/2\rangle \leftrightarrow |{}^{3}P_{0}, m_{F} = 9/2\rangle$ clock transition (denoted as $|g, 9/2\rangle \leftrightarrow |e, 9/2\rangle$ below). Further increasing the pulse duration results in a reduction of the excitation fraction but does not reduce the linewidth, primarily due to laser frequency noise. The atom-laser coherence is measured using Ramsey spectroscopy (Fig. 2b) by varying the relative phase between the two $\pi/2$ pulses. Even though the fringe contrast decays with a Gaussian time constant of 96(24) ms, where the value in brackets represents 1\sigma standard deviation, the variance of the excitation fractions remains large at 100 ms (Fig. 2b, inset (ii)), implying that the atoms within the ensemble remain phase coherent with each other for that interrogation time²⁷. The loss of atom-laser coherence is due to the finite coherence time of the clock laser and manifests itself as a randomized phase of the second $\pi/2$ pulse. However, when the two atomic ensembles are probed simultaneously, the relative atomic phase is preserved and is reflected in correlations between the excitation fractions of the two ensembles (Fig. 2c, inset). This can be further clarified in a parametric plot of the excitation fractions for

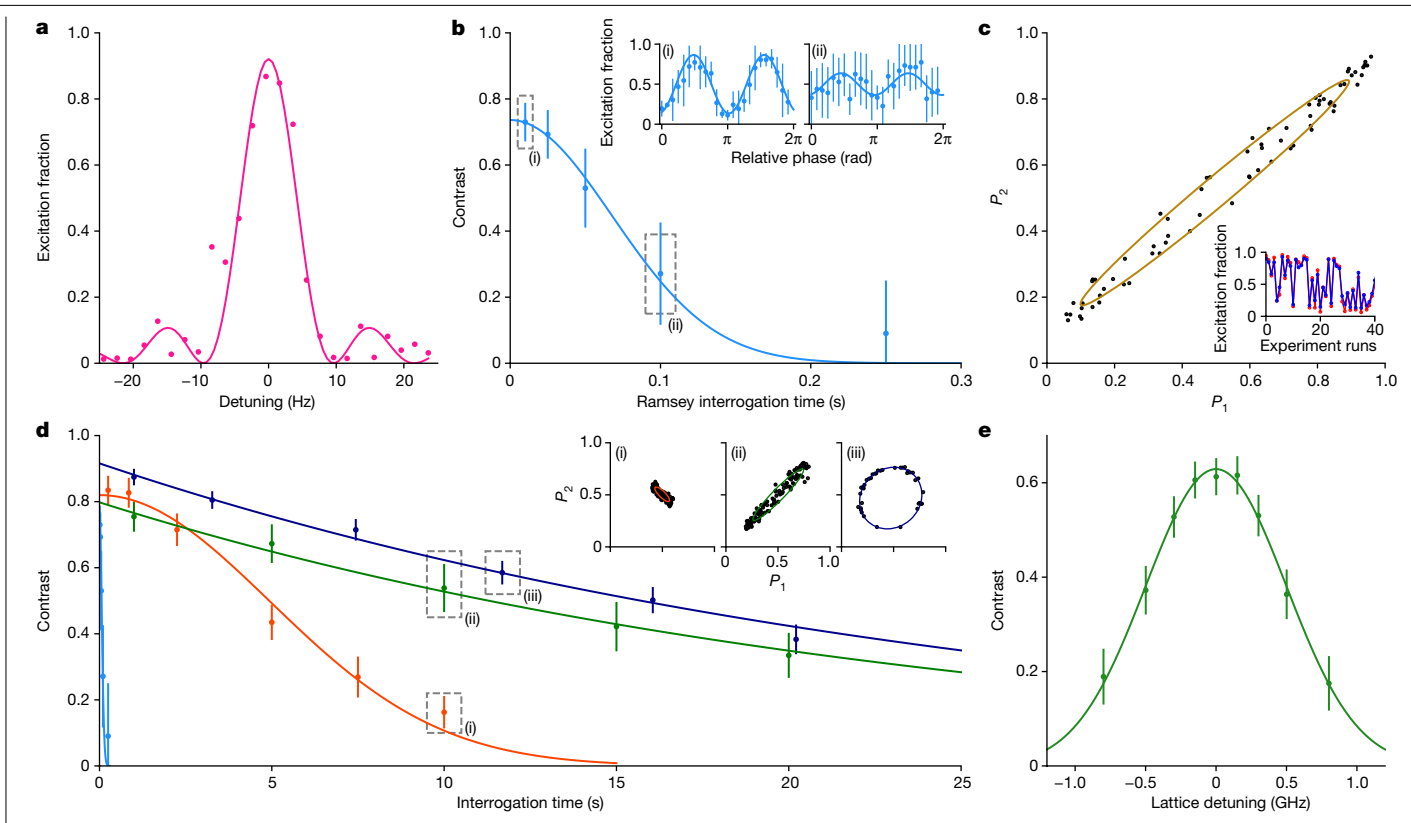


Fig. 2 | Characterization of atom-atom coherence time by synchronous **clock comparisons. a**, Rabi spectroscopy of a single ensemble with 90 ms π pulse duration (pink points) taken with one measurement without averaging. The fit gives a linewidth of 10.2(4) Hz (pink line). **b**, Decay of Ramsey contrast taken with one ensemble. This is fitted to a Gaussian envelope, which gives an atom-laser coherence time of 96(24) ms. Insets: Ramsey fringes at 10 (i) and 100 ms (ii) interrogation times. c, Parametric plot of excitation fractions in ensembles $1(P_1)$ and $2(P_2)$. Least-squares ellipse fitting (solid line) does not perform well at the phase near 0 or π due to QPN and the fit bias (Supplementary Information). Inset, correlations in P_1 (red) and P_2 (blue). d, Measurement of atom-atom coherence times for differential comparisons between two ensembles. Synchronous Ramsey interrogation of the $|^{1}S_{0}, m_{F} = 9/2\rangle \leftrightarrow |^{3}P_{0}, m_{F} = 9/2\rangle$ transition gives a 1/e coherence time of 6(1) s by

fitting to a Gaussian envelope (red line), whereas 'spin-echo' measurement using the same transition results in a 1/e decay time constant of 24(5) s (green line). Synchronous Ramsey interrogation of the magnetically less sensitive $|^{1}S_{0}, m_{F} = 5/2\rangle \leftrightarrow |^{3}P_{0}, m_{F} = 3/2\rangle$ transition results in a 26(2) s atom-atom coherence time (dark blue line). The decay of atom-laser coherence measured in **b** is shown for comparison (light blue line), but is barely visible on this scale. Insets: representative parametric plots illustrating relative contrast. e, The operational lattice magic wavelength for the $|^{1}S_{0}$, $m_{F} = 5/2 \Rightarrow |^{3}P_{0}$, $m_{F} = 3/2 \Rightarrow |^{3}P_{0}$ transition is found by measuring the contrast of synchronous Ramsey interrogations as a function of the lattice frequency detuning from 368,554.810(30) GHz. This is taken with a 10 s interrogation time and $20E_{\rm rec}$ lattice trap depth. The solid line is a Gaussian fit to the data.

ensembles 1 and 2, which fall on an ellipse with an opening angle determined by the differential Ramsey phase found between the two ensembles (Fig. 2c). By fitting an ellipse to the data, we extract the total accumulated phase difference modulo π (ref. ¹⁹).

The differential phase extracted from a fitted ellipse is a measure of the detuning between the two atomic ensembles. It contains information about all of the differential frequency shifts experienced by the spatially separated ensembles, including differential BBR shifts due to temperature gradients across the apparatus, differential linear and quadratic Zeeman shifts due to magnetic field gradients, differential d.c. Stark shifts due to electric field gradients, differential a.c. Stark shifts from the lattice and probe light due to differing field intensities at the two ensembles and the gravitational redshift due to general relativity. In our apparatus we find that the dominant shifts are the linear and quadratic Zeeman shifts due to the residual magnetic field gradient of B_x in the $\hat{\mathbf{z}}$ direction, which has an amplitude of about 15 mG cm⁻¹. At 1 cm this corresponds to a detuning between the $|g, 9/2\rangle \leftrightarrow |e, 9/2\rangle$ clock transitions of the two ensembles of 7.5 Hz, due to the differential linear Zeeman shift, and a differential quadratic Zeeman shift of 14 mHz at a bias field of 2 G.

To investigate the atom-atom coherence times, we perform synchronous Ramsey interrogation between the two ensembles. As pointed out in previous work^{27,32,37}, a shallow lattice trap depth is required for second-scale coherent interrogation to minimize Raman scattering out of the ${}^{3}P_{0}$ state 38 . We operate at a lattice depth of $20E_{rec}$ (where $Erec \approx h \times 3.5$ kHz is the lattice photon recoil energy, with h being Planck's constant) with a measured ${}^{3}P_{0}$ state lifetime of 13(2) s (Supplementary Information). However, when probing the $|g, 9/2\rangle \leftrightarrow |e, 9/2\rangle$ transition, we find that the contrast decays with a Gaussian time constant of 6(1) s, which is consistent with the expected inhomogeneous broadening due to the magnetic field gradient along $\hat{\mathbf{z}}$, corresponding to a frequency detuning of 150(10) mHz from the top to the bottom of the 200 µm spatial extent of each ensemble.

To confirm that the magnetic field gradient limits the atom-atom coherence time, we perform a 'spin-echo' measurement, and observe an exponential decay with a time constant of 24(5) s. To take full advantage of the availability of this longer coherence time, we therefore switch to interrogating the $|g, 5/2\rangle \leftrightarrow |e, 3/2\rangle$ transition, with a magnetic field sensitivity of about 22.4 Hz G⁻¹, which is 22 times smaller than that of the $|g, 9/2\rangle \leftrightarrow |e, 9/2\rangle$ transition^{5,39}. For this transition, the magnetic field gradient across each ensemble can be expected to contribute a detuning of only 7(1) mHz, and therefore the gradient no longer contributes dephasing on time scales limited by the Raman scattering.

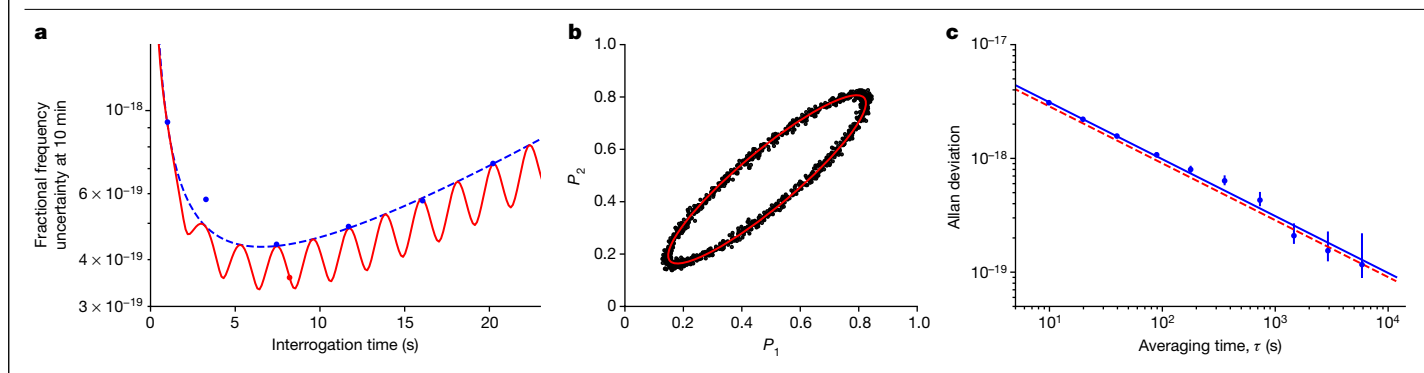


Fig. 3 | Low relative instability with multiplexed Ramsey interrogation. a, Measured fractional frequency uncertainties after 10 min of averaging (blue points) by choosing interrogation times T such that the differential phase ϕ_a is close to an odd multiple of $\pi/2$. The blue dashed line represents the expected QPN limit at a fixed offset phase $\pi/2$. The red solid line represents the QPN accounting for $\phi_d = 2\pi\delta f_{21} T$, where δf_{21} is the frequency detuning between two ensembles. The oscillation arises because QPN is maximized at a differential phase of $\pi/2$ and minimized at 0 or π (Supplementary Information). b, Parametric plots of P_2 versus P_1 (black points) with 1,193 experimental runs

for a total measurement time of 11,800 s. This is taken at T=8.205 s (the red point in $\mathbf a$) at a lattice trap depth of $20E_{\rm rec}$. A least-squares method (Supplementary Information) is used to fit an ellipse to the data (red line). $\mathbf c$, The corresponding Allan deviation (blue points) is extracted via jackknifing ^{19,27}. The differential clock comparison averages down with an instability of $9.7(4)\times 10^{-18}/\sqrt{\tau}$ (blue solid line), which matches the QPN limit (red dashed line) for the independently measured number of atoms in each ensemble ($N\approx 2400$), and reaches a relative statistical uncertainty of 8.9×10^{-20} after 3.3 h of averaging.

Due to the tensor a.c. Stark shift, the $|g, 5/2\rangle \leftrightarrow |e, 3/2\rangle$ transition will have a different operational magic wavelength, in which the scalar and tensor a.c. Stark shifts sum to zero, from the $|g, 9/2\rangle \leftrightarrow |e, 9/2\rangle$ transition (Supplementary Information). By scanning the lattice laser frequency over a range of ±800 MHz, we find a lattice frequency that maximizes the contrast for the $|g, 5/2\rangle \leftrightarrow |e, 3/2\rangle$ transition at 368,554.810(30) GHz (Fig. 2e), where the uncertainty comes from both the error in the Gaussian fitting and the accuracy of our wavemeter (10 MHz). We observe a 1/e atom-atom coherence time of 26(2) s for the $|g, 5/2\rangle \leftrightarrow |e, 3/2\rangle$ transition (Fig. 2d), which is consistent with the 'spin-echo' measurement for the $|g, 9/2\rangle \leftrightarrow |e, 9/2\rangle$ transition, and is roughly twice the measured clock state lifetime, implying that our results are primarily limited by Raman scattering. We note that here the atom-atom coherence time refers only to the lifetime of the synchronous Ramsey contrast for atoms remaining in the lattice at the end of the experiment, and therefore that time does not include atom loss due to heating and background gas collisions.

To characterize the relative instability of the multiplexed OLC, we perform a synchronous clock comparison between two ensembles separated by 0.6 cm with the $|g, 5/2\rangle \leftrightarrow |e, 3/2\rangle$ transition. Due to competition between the decay of contrast from Raman scattering out of the clock state and $1/\sqrt{T}$ scaling of QPN, the optimal interrogation time can be found by comparing the fractional frequency uncertainties at different interrogation times (Fig. 3a, blue points), which are chosen such that the differential phase ϕ_d is close to an odd multiple of $\pi/2$ to minimize biased error from ellipse fitting 19,27. The measurement agrees with the QPN limit at a fixed differential phase of $\pi/2$ (Fig. 3a, blue dashed line), which suggests an optimal interrogation time T at 7.5 s. However, due to the phase evolution of $\phi_d = 2\pi \delta f_{21} T$ at a comparable time scale to the interrogation times, where δf_{21} is the frequency difference between two ensembles, an additional differential -phase-dependent scale factor must be included in the expected QPN limit when the contrast is below 1 (Supplementary Information). As a result, the QPN is maximized when the ellipse phase is at $\pi/2$ and is minimized at 0 or π . This implies that one can benefit in sensitivity by trading off reduced QPN for increased bias in the ellipse fitting (Fig. 3a, red line). Therefore, we choose T = 8.205 s so that the phase of the ellipse is at about 0.44 rad, at which level the biased error is bounded to below 3% and can be easily compensated for (Supplementary Information). Figure 3b shows a measurement taken with 1,193 experiment runs recorded over 3.3 h and the corresponding fitted ellipse. The fit yields a net phase shift of about 12.130(2) rad or a frequency difference of 235.29(4) mHz between the two ensembles. The overlapping Allan deviation is computed and plotted in Fig. 3c, with a relative instability of $9.7(4)\times 10^{-18}/\sqrt{\tau}$, which is in agreement with the QPN limit (red dashed line), and a relative statistical uncertainty of 8.9×10^{-20} at the full 3.3 h of averaging time. This demonstration of relative precision below the 10^{-19} level with a rack-mounted, commercially available local oscillator with an instability of 1×10^{-15} at 1 s is encouraging for future applications that require portable or spaced-based clocks, such as relativistic geodesy and gravitational wave detection $^{7.14-16}$.

We demonstrate the scalability of the multiplexed OLC technique by moving from pairs to larger numbers of ensembles. This is achieved by modifying the sequence shown in Fig. 1b and repeating the lattice loading–moving cycle several times. A representative image is shown in Fig. 4a, in which six ensembles are equally distributed with 0.2 cm spacing. Each ensemble has about 500 atoms and the total lattice loading time is less than 100 ms. Synchronous interrogation and read-out result in 15 unique pairwise clock comparisons from a miniature network consisting of 6 'clocks' (Fig. 4b). Each comparison averages down with a slope below $3\times 10^{-17}/\sqrt{\tau}$, and reaches a relative statistical uncertainty of roughly 5×10^{-19} after 1 h of averaging. A 'closed-loop' analysis is performed to verify the self-consistency of the resulting differential frequencies. Good agreement of the scaled uncertainties for the 197 unique 'closed-loops' validate the precision of excitation–correlation comparisons using ellipse fitting (Fig. 4c).

The measured detunings between the ensemble pairs contain information about the spatial profiles of the thermal gradient, magnetic field gradient, electric field gradient and lattice beam, as well as the residual differential shifts due to differences in the atomic density and temperature between the ensembles. As an example, we evaluate the differential density shifts between ensemble pairs by varying the relative atom numbers, and thus the differential density (Methods). At a typical lattice trap depth of $20E_{\rm rec}$ and a conservative 100(25) atom number difference, the differential density shift is $-8(2)\times 10^{-19}$. This example highlights the effectiveness of the multiplexed technique for mapping out and evaluating systematic effects^{19,34}. A thorough evaluation of all of the contributing differential systematic shifts in our apparatus is currently underway.

Finally, precision isotope shift measurements have recently been proposed as an effective method to search for new physics beyond the Standard Model⁴⁰⁻⁴⁴. Neutral strontium, with four stable isotopes

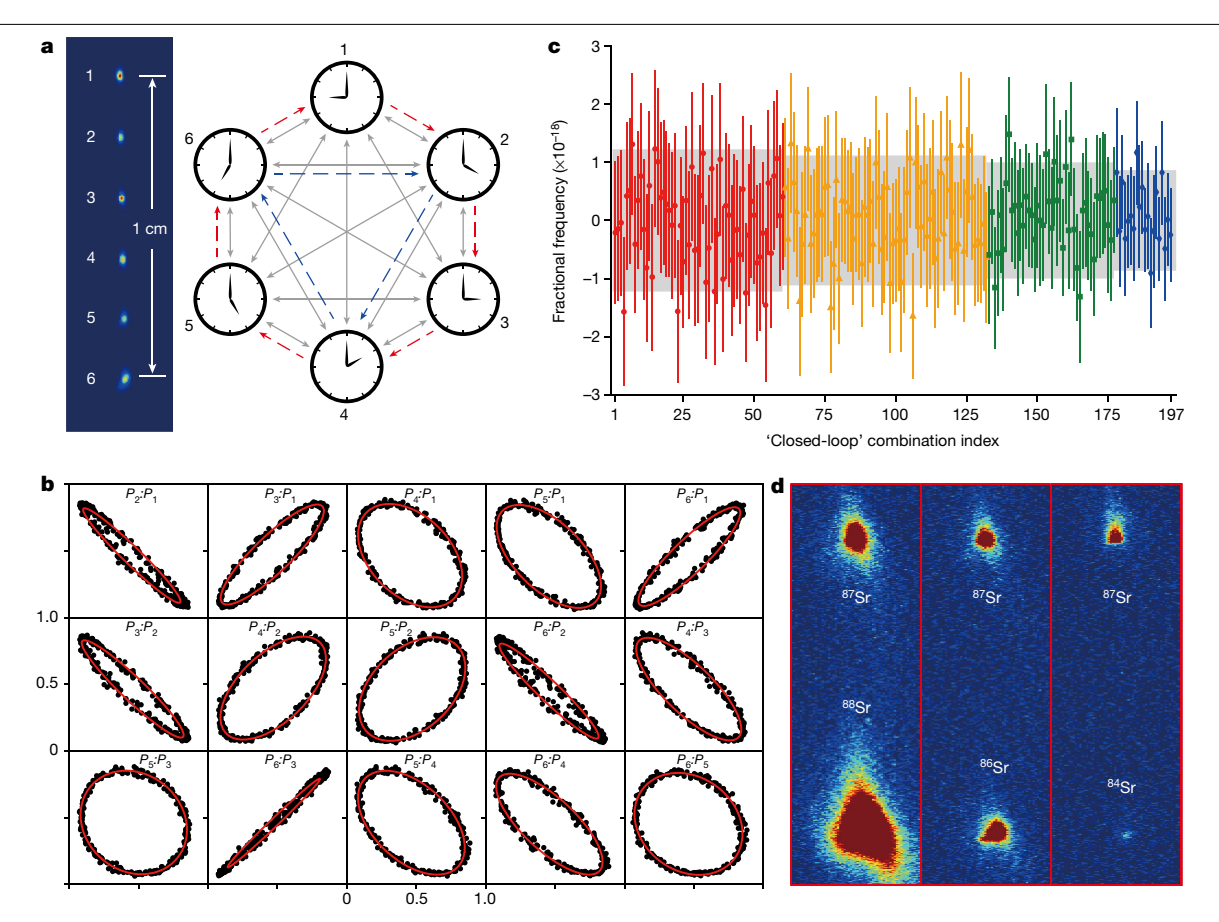


Fig. 4 | Prospects for multiplexed OLC comparisons. a, Camera image of 6 equally spaced ensembles loaded and interrogated simultaneously, which corresponds to 15 unique pairwise differential clock comparisons (grey double arrows with solid lines). The red arrows with dashed lines form a representative 'closed-loop' consisting of 6 ensembles, and the blue arrows with dashed lines form a 'closed-loop' of 3 ensembles. b, Parametric plots for all 15 pairwise comparisons with 6 ensembles taken at T = 8.5 s and a lattice trap depth of $20\textit{E}_{\text{rec}}.$ Each comparison averages down to a relative uncertainty of about 5×10^{-19} in 1 h. c, 'Closed-loop' analysis of 15 pairwise comparisons as a self-consistency check. Each data point corresponds to the summed differential frequency of the pairwise comparisons in the loop. This includes a

total of 197 unique loops with 6 ensembles (red, 60 combinations), 5 ensembles (orange, 72 combinations), 4 ensembles (green, 45 combinations) and 3 ensembles (blue, 20 combinations). The shaded grey areas represent uncertainty windows of 5×10^{-19} scaled by $\sqrt{6}$, $\sqrt{5}$, $\sqrt{4}$ and $\sqrt{3}$, respectively. d. Demonstration of simultaneous loading of spatially resolved heterogeneous pairs of isotopes in a single experiment run (three separate representative experiments are shown covering all four stable isotopes of Sr). Each isotope in a $pair is imaged individually \, by \, shifting \, the \, 461 \, nm \, probe \, beam \, onto \, resonance$ sequentially. The colour map is kept on the same scale for all three images, with the atom numbers for the bosonic isotopes consistent with their relative isotopic abundance (88Sr, 82.6%; 87Sr, 6.9%; 86Sr, 9.9%; 84Sr, 0.6%).

(88Sr, 87Sr, 86Sr and 84Sr) and narrow-line clock transitions, is a good candidate for these studies, particularly when combined with measurements of the clock transitions in the Sr⁺ ion ⁴¹. We therefore demonstrate the ability to sequentially load different spatially resolved strontium isotopes into the lattice with pairs comprising all four stable isotopes of strontium (Fig.4d). Due to the lack of hyperfine states for bosonic isotopes, a greater magnetic field (around 20 G) is required to mix a small component of the ${}^{3}P_{1}$ state in with the ${}^{3}P_{0}$ state 27,37,45,46 and allow the doubly forbidden ${}^{1}S_{0} \leftrightarrow {}^{3}P_{0}$ clock transition. In addition, each isotope will have its own magic wavelength, requiring new techniques for evaluating or reducing differential lattice light shifts and broadening⁴². We therefore leave multiplexed comparisons between Sr isotopes for future work.

In conclusion, in this work we demonstrate a new platform for differential clock comparisons using spatially resolved atomic ensembles trapped in a single 1D optical lattice. We demonstrate long atomic coherence times (26 s) with large atom numbers (2,400 atoms per ensemble) in a shallow ($20E_{rec}$) vertical optical lattice using a hertz-linewidth clock laser. In a comparison between two ensembles, we achieve a relative instability of $9.7(4) \times 10^{-18} / \sqrt{\tau}$, which is consistent with the QPN limit, and a relative statistical uncertainty of 8.9×10^{-20} after 3.3 h of averaging. We take advantage of the multiplexed nature of our apparatus to demonstrate a miniaturized clock network consisting of 6 atomic ensembles, resulting in 15 unique pairwise clock comparisons with relative instabilities below $3 \times 10^{-17} / \sqrt{\tau}$. We also demonstrate the ability to simultaneously load heterogeneous pairs of all four stable isotopes of strontium into spatially resolved ensembles in the lattice. Common-mode rejection of dephasing from the local oscillator noise and environmental fluctuations mean that the multiplexed OLC platform is well-suited for exploring the use of spin-squeezing to push the relative instability below the QPN limit ^{33,47,48}. Full characterization of systematic effects such as differential BBR and Zeeman and Stark shifts will enable measurements of the gravitational redshift at the subcentimetre scale and other new tabletop tests of relativity. We anticipate that this technique can be straightforwardly applied to other existing OLCs, providing a new tool for the evaluation of limiting systematics, including the spatial mapping of thermal, magnetic and electric gradients, in some of the world's most accurate clocks.

Finally, we note that, while performing the work described here, we became aware of complementary work in which differential clock comparisons with record relative instability and precision were performed between subregions within a single millimetre-scale atomic ensemble in a vertical 1D lattice. An ultra-narrow linewidth local oscillator stabilized

to a cryogenic single-crystal silicon cavity was used, enabling observation of the gravitational redshift across the ensemble⁴⁹. Combined with the multiplexed clock technique demonstrated here, these results are promising for future precision tests of relativity at the millimetre to centimetre scale.

Online content

Any methods, additional references, Nature Research reporting summaries, source data, extended data, supplementary information, acknowledgements, peer review information; details of author contributions and competing interests; and statements of data and code availability are available at https://doi.org/10.1038/s41586-021-04344-y.

- Ludlow, A. D., Boyd, M. M., Ye, J., Peik, E. & Schmidt, P. O. Optical atomic clocks. Rev. Mod. Phys. 87, 637-701 (2015).
- 2 Campbell, S. L. et al. A Fermi-degenerate three-dimensional optical lattice clock. Science 358. 90-94 (2017).
- McGrew, W. F. et al. Atomic clock performance enabling geodesy below the centimetre level, Nature 564, 87-90 (2018).
- Δ Schioppo, M. et al. Ultrastable optical clock with two cold-atom ensembles. Nat. Photon. 11, 48-52 (2017).
- 5 Oelker, E. et al. Demonstration of 4.8×10^{-17} stability at 1s for two independent optical clocks. Nat. Photon. 13, 714-719 (2019).
- Safronova, M. S. et al. Search for new physics with atoms and molecules. Rev. Mod. Phys. 90, 025008 (2018).
- Kolkowitz, S. et al. Gravitational wave detection with optical lattice atomic clocks. Phys. Rev. D 94, 124043 (2016).
- Stadnik, Y. V. & Flambaum, V. V. Improved limits on interactions of low-mass spin-O dark matter from atomic clock. spectroscopy. Phys. Rev. A 94, 022111 (2016).
- Derevianko, A. & Pospelov, M. Hunting for topological dark matter with atomic clocks. Nat. Phys. 10, 933-936 (2014).
- Arvanitaki, A., Huang, J. W. & Van Tilburg, K. Searching for dilaton dark matter with atomic clocks. Phys. Rev. D 91, 015015 (2015).
- Wcisło, P. et al. New bounds on dark matter coupling from a global network of optical atomic clocks. Sci. Adv. 4, eaau4869 (2018).
- Kennedy, C. J. et al. Precision metrology meets cosmology: improved constraints on ultralight dark matter from atom-cavity frequency comparisons. Phys. Rev. Lett. 125. 201302 (2020).
- Chou, C. W., Hume, D. B., Rosenband, T. & Wineland, D. J. Optical clocks and relativity. Science 329, 1630-1633 (2010).
- 14. Takano, T. et al. Geopotential measurements with synchronously linked optical lattice clocks, Nat. Photon, 10, 662-666 (2016).
- Grotti, J. et al. Geodesy and metrology with a transportable optical clock. Nat. Phys. 14, 15. 437-441 (2018).
- 16. Takamoto, M. et al. Test of general relativity by a pair of transportable optical lattice clocks. Nat. Photon. 14, 411-415 (2020).
- Hinkley, N. et al. An atomic clock with 10⁻¹⁸ instability. Science **341**, 1215–1218 (2013).
- Bloom, B. J. et al. An optical lattice clock with accuracy and stability at the 10^{-18} level. 18. Nature 506, 71-75 (2014).
- Marti, G. E. et al. Imaging optical frequencies with 100 μ Hz precision and 1.1 μ m resolution. Phys. Rev. Lett. 120, 103201 (2018).
- Bothwell, T. et al. JILA SrI optical lattice clock with uncertainty of 2.0×10^{-18} . Metrologia
- Boulder Atomic Clock Optical Network (BACON) Collaboration. Frequency ratio measurements at 18-digit accuracy using an optical clock network. Nature 591, 564-569
- Itano, W. M. et al. Quantum projection noise: population fluctuations in two-level systems. Phys. Rev. A 47, 3554 (1993).

- Dick, G. J., Prestage, J. D., Greenhall, C. A. & Maleki, L. Local oscillator induced degradation of medium-term stability in passive atomic frequency standards. In Proc. 22nd Precise Time and Time Interval Meeting (Ed.Sydnor, R. L.) 487-508 (NASA, 1990).
- Kim, M. E. et al. Optical coherence between atomic species at the second scale: improved clock comparisons via differential spectroscopy. Preprint at https://arxiv.org/ abs/2109.09540 (2021).
- Nicholson, T. L. et al. Comparison of two independent Sr optical clocks with 1 × 10⁻¹⁷ stability at 10³ s. Phys. Rev. Lett. **109**, 230801 (2012).
- Clements, E. R. et al. Lifetime-limited interrogation of two independent ²⁷Al* clocks using correlation spectroscopy. Phys. Rev. Lett. 125, 243602 (2020).
- Young, A. W. et al. Half-minute-scale atomic coherence and high relative stability in a tweezer clock. Nature **588**, 408-413 (2020).
- 28. Matei, D. G. et al. 1.5 μ m lasers with sub-10 mHz linewidth. *Phys. Rev. Lett.* **118**, 263202 (2017).
- 29. Swallows, M. D. et al. Suppression of collisional shifts in a strongly interacting lattice clock. Science 331, 1043-1046 (2011).
- Martin, M. J. et al. A quantum many-body spin system in an optical lattice clock. Science 30. 341, 632-636 (2013).
- Blatt, S. et al. Rabi spectroscopy and excitation inhomogeneity in a one-dimensional optical lattice clock. Phys. Rev. A 80, 052703 (2009).
- 32 Hutson, R. B. et al. Engineering quantum states of matter for atomic clocks in shallow optical lattices. Phys. Rev. Lett. 123, 123401 (2019).
- Pedrozo-Peñafiel, E. et al. Entanglement on an optical atomic-clock transition. Nature 588, 414-418 (2020).
- Beloy, K. et al. Faraday-shielded dc stark-shift-free optical lattice clock. Phys. Rev. Lett. 120, 183201 (2018).
- Zhang, W. et al. Ultrastable silicon cavity in a continuously operating closed-cycle cryostat at 4K. Phys. Rev. Lett. 119, 243601 (2017).
- Milner, W. R. et al. Demonstration of a timescale based on a stable optical carrier. Phys. Rev. Lett. 123, 173201 (2019).
- Norcia, M. A. et al. Seconds-scale coherence on an optical clock transition in a tweezer array. Science 366, 93-97 (2019)
- 38. Dörscher, S. et al. Lattice-induced photon scattering in an optical lattice clock. Phys. Rev.
- Boyd, M. M. et al. Nuclear spin effects in optical lattice clocks. Phys. Rev. A 76, 022510
- 40. Delaunay, C., Ozeri, R., Perez, G. & Soreq, Y. Probing atomic Higgs-like forces at the precision frontier. Phys. Rev. D 96, 093001 (2017).
- Berengut, J. C. et al. Probing new long-range interactions by isotope shift spectroscopy. Phys. Rev. Lett. 120, 091801 (2018).
- Takano, T., Mizushima, R. & Katori, H. Precise determination of the isotope shift of 88Sr 87Sr optical lattice clock by sharing perturbations. Appl. Phys. Express 10, 072801 (2017).
- Miyake, H., Pisenti, N. C., Elgee, P. K., Sitaram, A. & Campbell, G. K. Isotope-shift spectroscopy of the ${}^{1}S_{0} \rightarrow {}^{3}P_{1}$ and ${}^{1}S_{0} \rightarrow {}^{3}P_{0}$ transitions in strontium. Phys. Rev. Res. 1, 033113 (2019).
- Counts, I. & Hur, J. et al. Evidence for nonlinear isotope shift in Yb⁺ search for new boson. Phys. Rev. Lett. 125, 123002 (2020).
- Taichenachev, A. V. et al. Magnetic field-induced spectroscopy of forbidden optical transitions with application to lattice-based optical atomic clocks. Phys. Rev. Lett. 96, 083001 (2006).
- Madjarov, I. S. et al. An atomic-array optical clock with single-atom readout. Phys. Rev. X 9, 041052 (2019).
- Gil, L. I. R., Mukherjee, R., Bridge, E. M., Jones, M. P. A. & Pohl, T. Spin squeezing in a Rydberg lattice clock. Phys. Rev. Lett. 112, 103601 (2014).
- Van Damme, J., Zheng, X., Saffman, M., Vavilov, M. G. & Kolkowitz, S. Impacts of random filling on spin squeezing via Rydberg dressing in optical clocks. Phys. Rev. A 103, 023106
- Bothwell, T. et al. Resolving the gravitational redshift within a millimeter atomic sample. Nature https://doi.org/10.1038/s41586-021-04349-7 (2022).

Publisher's note Springer Nature remains neutral with regard to jurisdictional claims in published maps and institutional affiliations.

© The Author(s), under exclusive licence to Springer Nature Limited 2022

Methods

Initial loading and trapping

The experiment begins by capturing atoms from a thermal atomic beam in a three-dimensional magneto-optical trap (MOT) operating on the $^1S_0 \rightarrow ^1P_1$ transition at 461 nm, which has a linewidth of 32 MHz. The atom number in the 461 nm MOT is typically 2×10^6 for 87 Sr, with a temperature of approximately 1 mK. The sample is further cooled by transfer from the 461 nm MOT into a 689 nm MOT through the 7.5 kHz wide $^1S_0 \leftrightarrow ^3P_1$ transition. After broad-band and single-frequency (SF) 689 nm MOT stages, about 2×10^5 atoms are left with a temperature of around 2 μ K. The optical lattice is kept on during the entire experiment, and about 1×10^5 spin-mixed atoms are transferred into the optical lattice by switching off the SF 689 nm MOT.

Movable lattice

A1D 'magic wavelength' lattice (λ_L = 813.4 nm) is formed using an incoming beam (1.5 W) focused to a 100 μ m beam waist and a retro-reflected beam with a matching waist. The lattice is orientated in the $\hat{\mathbf{z}}$ direction to suppress tunnelling with the help of gravity, which lifts the degeneracy between adjacent lattice sites so. The optical lattice light is generated by a Ti:Sapphire laser (Msquared SolsTiS), diffracted by an acousto-optic modulator (AOM) operating at 80 MHz, and the negative first diffraction order is delivered to the experiment table through a polarization-maintaining fibre. The lattice laser intensity is actively stabilized by monitoring the intensity of the lattice beam using a pick-off after the beam has initially passed through the science chamber and feeding back on the AOM before the fiber. The lattice laser frequency is digitally locked to a wavemeter (High-Finesse, WS-70) that is calibrated using the ${}^1S_0 \leftrightarrow {}^3P_0$ clock transition of 87 Sr, which is known to an accuracy below 1 Hz (ref. so

To realize the movable lattice 52 , the incoming lattice beam is reshaped with a pair of telescope lenses after the science chamber, and is then subsequently sent through two AOMs (lattice AOM1 and lattice AOM2) operating at ∓ 110 MHz (Extended Data Fig. 1). A 'cat's eye' retro-reflector consisting of a 100 mm lens and a high-reflection mirror is used to retro-reflect the lattice beam and double-pass the AOMs. The power of the retro-reflection beam is about 50% compared to the incoming beam and is mainly limited by the AOM diffraction efficiencies (approximately 90% per single pass) and the optical losses in the path.

In this configuration, the lattice retro-frequency $(\nu_L + \delta \nu_L)$ can be detuned from the incoming frequency (ν_L) by varying the radio-frequency drive of the second AOM. At zero detuning $(\delta \nu_L = 0)$, the lattice is a standing wave and the clock can be operated in the traditional fashion. A constant detuning $\delta \nu_L$ results in a moving lattice with a velocity ν

$$v = \frac{1}{2} \lambda_{\rm L} \delta v_{\rm L}. \tag{2}$$

If δv_1 is changed with time, the lattice will accelerate at

$$a = \frac{1}{2} \lambda_{L} (\partial \delta \nu_{L} / \partial t), \tag{3}$$

which in our apparatus can exceed 100g, and is mainly limited by the atomic temperature and lattice trap depth, where $g \approx 9.80$ m s⁻² is the acceleration due to gravity.

Two phase-synchronized direct digital synthesizers (Moglabs XRF421) are used to drive the lattice AOMs. To perform the lattice movement procedure, the direct digital synthesizer driving the lattice AOM 2 is programmed to step over 4,000 values for a 2 ms ramp with an update interval of 500 ns on receiving an external trigger signal. About 80% of the total atoms survive after the lattice acceleration and deceleration stages. We note that the 'cat's eye' configuration is critical

for ramping the lattice frequency while preserving the alignment of the retro-lattice, which is monitored through the rejection port of an optical isolator placed before the fibre. We observe negligible power loss when detuning the retro-lattice frequency by as much as $\pm 10~\mathrm{MHz}$, which is more than sufficient to prepare ensembles separated by 1 cm in the experiment in tens of milliseconds.

State preparation, cooling and read-out

For ⁸⁷Sr, a 689 nm laser beam propagating perpendicular to the lattice is applied to spin-polarize atoms into a $|^1S_0, m_F = \pm 9/2\rangle$ (denoted as $|g, \pm 9/2\rangle$) hyperfinestate manifold through the 689 nm $^1S_0 \leftrightarrow ^3P_1$ (F = 9/2) transition. We then perform in-lattice cooling both axially and radially on the same transition to remove phonons after lattice acceleration, and adiabatically ramp down the lattice trap depth from $60E_{\rm rec}$ to below $20E_{\rm rec}$, where $E_{\rm rec} \approx h \times 3.5$ kHz is the lattice photon recoil energy.

To prepare ensembles into $|^3P_0, m_F = \pm 3/2\rangle$ (denoted as $|e, \pm 3/2\rangle$) states, we coherently transfer the populations through three π pulses on resonance with the $|g, \pm 9/2\rangle \leftrightarrow |e, \pm 7/2\rangle$, $|e, \pm 7/2\rangle \leftrightarrow |g, \pm 5/2\rangle$, and $|g, \pm 5/2\rangle \leftrightarrow |e, \pm 3/2\rangle$ transitions (Extended Data Fig. 2). About 70% of atoms are transferred to the $|e, \pm 3/2\rangle$ state, and this figure is primarily limited by the π pulse fidelity.

To detect the excitation fraction of each ensemble in parallel, we first read out the 1S_0 ground-state populations with a 1 ms imaging pulse from a 461 nm laser beam co-propagating along the lattice, and then collect the atomic fluorescence using an electron multiplying charge-coupled device (Andor iXon-888). The imaging beam also removes the population in the ground state. The remaining populations in the 3P_0 excited state are simultaneously transferred back to the ground state by repump pulses tuned to the 679 nm ${}^3P_0 \leftrightarrow {}^3S_1$ and 707 nm ${}^3P_2 \leftrightarrow {}^3S_1$ transitions. A second imaging pulse is then applied to measure the populations. A reference image is taken with a final imaging pulse without any atoms for background subtraction. Excitation fractions of each ensemble can be extracted by post-selecting regions of interest in the images, and the normalized excitation fraction is given by $P_n = (N_{e,n} - N_{bg,n})/(N_{e,n} + N_{g,n} - 2N_{bg,n})$, where n refers to the nth ensemble, $N_{g/e}$ is the atom number in $|g\rangle/|e\rangle$ after calibration and N_{bg} is the background.

Clock laser beam path

The rack-mounted clock laser (Menlo Systems, Optical Reference System) is referenced by Pound-Drever-Hall locking to a 12 cm ULE cavity, which is temperature controlled at the zero-crossing point at 15.77 °C. A double-passed AOM before fibre coupling into the ULE cavity is used for linear drift cancellation. A typical linear drift rate from 0.2 to 1 Hz s⁻¹ is observed for the ULE cavity, and a residual drift of about 0.01 Hz s⁻¹ can be achieved on calibration based on the clock transition resonance. The clock laser beam is delivered to the experiment table through a 5 m polarization-maintaining fibre, with an output power of approximately 2 mW. The clock beam is then diffracted by an AOM (clock AOM) operating at +110 MHz to steer the laser frequency to be on resonance with the ${}^{1}S_{0} \leftrightarrow {}^{3}P_{0}$ clock transition. The clock beam is focused down to a beam waist of about 500 µm centred on the lattice, which is about 5 times the value of the lattice beam waist to both ensure homogeneity for atoms populated radially and multiple ensembles distributed axially along the lattice.

To cancel fibre phase noise and residual Doppler noise induced by vibrations of the fibre and the optical lattice, the zeroth diffraction order of the clock AOM is referenced on the lattice retro-reflection mirror ^{53,54}. To excite the $|g,9/2\rangle\leftrightarrow|e,9/2\rangle\pi$ transition, the first diffraction order is overlapped with the lattice beam by first using a long-pass dichroic beam splitter and subsequently transmitting through the polarized beam splitter. To excite the $|g,5/2\rangle\leftrightarrow|e,3/2\rangle\sigma$ transition, the clock beam is overlapped with the lattice beam through the reflection port of the polarized beam splitter. This

difference in lattice and clock beam polarization is adopted due to the orthogonal polarizations needed to excite the π and σ transitions using a linearly polarized clock beam (see the inset of Extended Data Fig. 1 for details). Even though this configuration leaves an uncompensated lattice path of about 75 cm, we observe no significant effect on the measured instabilities as inferred from the synchronous Ramsey interrogations.

Clock interrogations

The clock transition is interrogated under a bias magnetic field of approximately 2 G. The first diffraction order of the clock AOM is used to address the clock resonance. To circumvent thermal effects in the AOM crystal, the clock pulses are generated by jumping the AOM frequency from 10 MHz off-resonant to on-resonant, instead of switching the clock AOM on and off. Shifting the clock AOM frequency by 10 MHz induces a differential Bragg diffraction angle that gives a deflection of more than 0.5 cm at the ensembles. This transverse spatial offset, in addition to an optical shutter that blocks any residual clock light, ensures the clock beam is not incident on the atoms during clock interrogation.

The Rabi spectroscopy image shown in Fig. 2a is taken of the $|g,9/2\rangle\leftrightarrow|e,9/2\rangle$ transition at a lattice trap depth of $20E_{rec}$, and with a π pulse duration of about 90 ms, which corresponds to Rabi frequency of $2\pi\times5.6$ Hz. A neutral-density filter (3.5 optical density) is used to attenuate the clock beam power and ensure the resulting Rabi linewidth remains Fourier limited. The data are taken in a total measurement time of less than a minute without averaging.

For Ramsey spectroscopy and 'spin-echo' measurement of the $|g, 9/2\rangle \leftrightarrow |e, 9/2\rangle$ transition, the $\pi/2$ pulse duration is about 0.75 ms (a Rabi frequency of $2\pi \times 333$ Hz). For Ramsey spectroscopy of the $|g,5/2\rangle \leftrightarrow |e,3/2\rangle$ transition, initial state preparation is achieved using three consecutive π pulses of about 4.5, 3.5 and 3.0 ms (Rabi frequencies of $2\pi \times 111$ Hz, $2\pi \times 142$ Hz and $2\pi \times 167$ Hz) to address the $|g, 9/2\rangle \leftrightarrow |e, 7/2\rangle$, $|e, 7/2\rangle \leftrightarrow |g, 5/2\rangle$ and $|g, 5/2\rangle \leftrightarrow |e, 3/2\rangle$ transitions, respectively. The difference in pulse durations is a result of the different matrix elements for the three transitions. Each π pulse is followed by a 'clean-up' pulse on resonance with the ${}^{1}S_{0} \leftrightarrow {}^{1}P_{1}$ transition (${}^{3}P_{0} \leftrightarrow {}^{3}S_{1}$ and ${}^{3}P_{2} \leftrightarrow {}^{3}S_{1}$ repump transitions) to remove any remaining population from the ground (clock) state due to imperfect spin-polarization and π pulses. The nearby clock resonances from the final $|e, 3/2\rangle$ state, for example, the $|g.3/2\rangle \leftrightarrow |g.3/2\rangle$ and $|g.3/2\rangle \leftrightarrow |g.1/2\rangle$ transitions, can be eliminated by applying both a large bias magnetic field to induce larger separation between the σ^+ and σ^- transitions, and fine alignment of the bias field orientation to suppress the unwanted π transition. After preparing atoms in the $|e, 3/2\rangle$ state, Ramsey spectroscopy images are taken with $\pi/2$ pulses of 1.5 ms duration and interrogation times of up to 20 s.

Experimental procedure

The procedure and timing diagram for loading, lattice acceleration, cooling, clock interrogation and imaging is shown in Extended Data Fig. 3. It takes 400 ms to load thermal atoms into the 461 nm MOT, 450 ms to cool the atoms in the broad-band 689 nm MOT and 50 ms to further cool them down to around 2 µK by holding them in the SF 689 nm MOT. In the SF 689 nm MOT stage, the lattice is accelerated by linearly ramping the lattice AOM 2 frequency to load multiple ensembles in less than 100 ms. This is then followed by spin-polarization, in-lattice cooling and adiabatic ramping down of the lattice trap depth in less than 200 ms. An extra 100 ms is spent on coherent transfer from the $|g, 9/2\rangle$ to the $|e, 3/2\rangle$ state when interrogating the $|g, 5/2\rangle \leftrightarrow |e, 3/2\rangle$ transition. The imaging subsequence usually takes about 150 ms. The above sample trapping, loading, cooling, state preparation and read-out times contribute to a typical dead time of 1.6 s per experimental cycle. This yields an 84% duty cycle for an 8.205 s synchronous Ramsey interrogation.

Coherence times

Ramsey spectroscopy with a single ensemble is performed to measure the atom–laser coherence time. The averaged excitation fraction is fitted to a sinusoidal function (Fig. 2b, insets (i) and (ii)) and the corresponding amplitude is extracted as the contrast at each interrogation time. The contrast is then fitted to a Gaussian envelope to extract the coherence time³⁷. To measure the atom–atom coherence times, synchronous Ramsey interrogations and 'spin-echo' measurements are performed between two ensembles. The contrasts extracted from the resulting ellipses (Supplementary Information) are used to determine the coherence times.

Specifically, a fit to a Gaussian envelope is chosen for Ramsey spectroscopy with one ensemble due to decoherence from the local oscillator noise. The same fit applies for synchronous Ramsey interrogation with two ensembles of the $\lfloor g,9/2 \rangle \leftrightarrow \lfloor e,9/2 \rangle$ transition as inhomogeneous broadening from a residual magnetic field gradient across each ensemble limits the coherence time. Exponential fittings are used for the 'spin-echo' measurement on the $\lfloor g,9/2 \rangle \leftrightarrow \lfloor e,9/2 \rangle$ transition and synchronous Ramsey interrogation of the $\lfloor g,5/2 \rangle \leftrightarrow \lfloor e,3/2 \rangle$ transition, as these methods are primarily limited by the finite lifetime of the clock state due to Raman scattering³⁸.

A summary of the measured coherence times is shown in Extended Data Table 1.

Ellipse fitting bias correction

To determine the differential phase ϕ_d between ensemble pairs accumulated during the clock interrogation, a least-squares method is applied for ellipse fitting (see Supplementary Information for details). Even though this approach is numerically stable, non-iterative and guarantees an ellipse-specific solution, it does not perform well at ϕ_d close to 0 or π (ref. ²⁷). Moreover, the effective probability distribution that the data is sampled from is the convolution of an ellipse and a binomial distribution associated with the QPN. Therefore, the bias error needs to be accounted for to extract the correct differential frequencies between the ensemble pairs. To do this, we perform Monte-Carlo simulations that generate artificial data that capture QPN by using specific contrast, and atom number and differential phases as input parameters. The simulated data enable us to calculate a bias-corrected phase with a statistical standard deviation (s.d.) as the error bar in the bias correction.

To illustrate the validity and importance of bias correction, a comparison of the 'closed-loop' analysis in Fig. 4c with and without bias correction is shown in Extended Data Fig. 4. The sum frequencies of each unique 'closed-loop' agree in a 1×10^{-18} window with bias correction, whereas the deviations from zero are as large as 1×10^{-17} without bias correction. The corresponding extracted differential frequencies after bias correction are listed in Extended Data Table 2. We note that whereas this bias can be avoided through a judicious choice of phase for two clocks, it is unavoidable in differential clock comparisons with three or more clocks. For example, consider the extreme case in which two pairs of clocks are operating at differential phases of odd multiples of $\pi/2$ and the bias error is minimized, that is, $\phi_{12}=(2m+1)\pi/2$ and $\phi_{23}=(2n+1)\pi/2$, where m and n are integers. The outcome of the third pair would be $\phi_{13}=\phi_{12}+\phi_{23}=((m+n)+1)\pi$, which is a multiple of π when the bias error is maximized.

Differential density shift

The differential density shift is evaluated by varying the atom number difference between symmetrically trapped ensemble pairs. This is accomplished by first balancing the lattice trap depths and radial profiles at each ensemble by optimizing the lattice alignment, which is verified through motional sideband spectroscopy. The loading times for each ensemble are then varied from 0.5 ms to 20 ms to introduce atom number differences between the ensembles (typically within the

range of $\pm 2,000$ atoms), yielding shifts at the 10^{-18} level. The motional sideband spectroscopy is performed again to ensure the temperatures of the two ensembles remain balanced after in-lattice cooling. The spatial gradient of the fluorescence collected on the electron multiplying charge-coupled device is also calibrated using a movable ensemble (Supplementary Information).

'Lock-in' type measurements are performed by varying the relative atom numbers, ΔN . The resulting relative phase shifts $\Delta \phi$ are then used to extract the differential density shift. A linear function $a\Delta N + b$ is used to fit the data, where a and b are fit parameters, and the slope a is extracted as the differential density shift per 100 atom number difference (Extended Data Fig. 5a).

To quantify the scaling of the differential density shift with lattice trap depth U, the 'lock-in' measurement is taken at different lattice trap depths and the fitted slopes are plotted as a function of U (Extended Data Fig. 5b). The data are then fitted to the model $\alpha U^{5/4} + \beta$, where α and β are fit parameters. The good agreement between the data and $U^{5/4}$ scaling implies that the axial and radial trap frequencies in the 1D lattice scale with trap depth, as is expected for a thermal gas^{20,55}.

Units and errors

Unless otherwise stated, all errors and numerical uncertainties in this article and its Supplementary Information denote a 1σ s.d. confidence interval. When we quote a coherence time, we are typically referring to the 1/e decay time. When we explicitly refer to a Gaussian time constant, we are referring to the time scale associated with 1 s.d. of the Gaussian envelope.

Data availability

The experimental data presented in this manuscript are available from the corresponding author upon reasonable request. Source data are provided with this paper.

Code availability

The code used for experimental control, data analysis and simulation in this work are available from the corresponding author upon reasonable request.

- Lemonde, P. & Wolf, P. Optical lattice clock with atoms confined in a shallow trap. Phys. Rev. A 72, 033409 (2005).
- Campbell, G. K. et al. The absolute frequency of the ⁸⁷Sr optical clock transition. *Metrologia* 45, 539 (2008).
- 52. Schmid, S., Thalhammer, G., Winkler, K., Lang, F. & Denschlag, J. H. Long distance transport of ultracold atoms using a 1D optical lattice. *New J. Phys.* **8**, 159 (2006).
- Ma, L. S., Jungner, P., Ye, J. & Hall, J. L. Delivering the same optical frequency at two
 places: accurate cancellation of phase noise introduced by an optical fiber or other
 time-varying path. Opt. Lett. 19, 1777–1779 (1994).
- Falke, S., Misera, M., Sterr, U. & Lisdat, C. Delivering pulsed and phase stable light to atoms of an optical clock. Appl. Phys. B 107, 301–311 (2012).
- Swallows, M. D. et al. Operating a ⁸⁷Sr optical lattice clock with high precision and at high density. *IEEE Trans. Ultrason. Ferroelectr. Freq. Control.* 59, 416–425 (2012).

Acknowledgements We thank J. Ye, A. Kaufman, J. Thompson, T. Bothwell and A. Jayich for insightful discussions and helpful feedback on the manuscript. This work was supported in part by the NIST Precision Measurement Grants program, the Northwestern University Center for Fundamental Physics and the John Templeton Foundation through a Fundamental Physics grant, the Wisconsin Alumni Research Foundation, the Army Research Office through agreement number W911NF-21-1-0012 and a Packard Fellowship for Science and Engineering.

Author contributions X.Z. designed and built the experimental apparatus with assistance from J.D., V.L., H.L. and B.N.M., and with guidance from S.K. All authors contributed to maintenance and operation of the experimental apparatus, data collection, data analysis and writing of the manuscript

Competing interests The authors declare no competing interests.

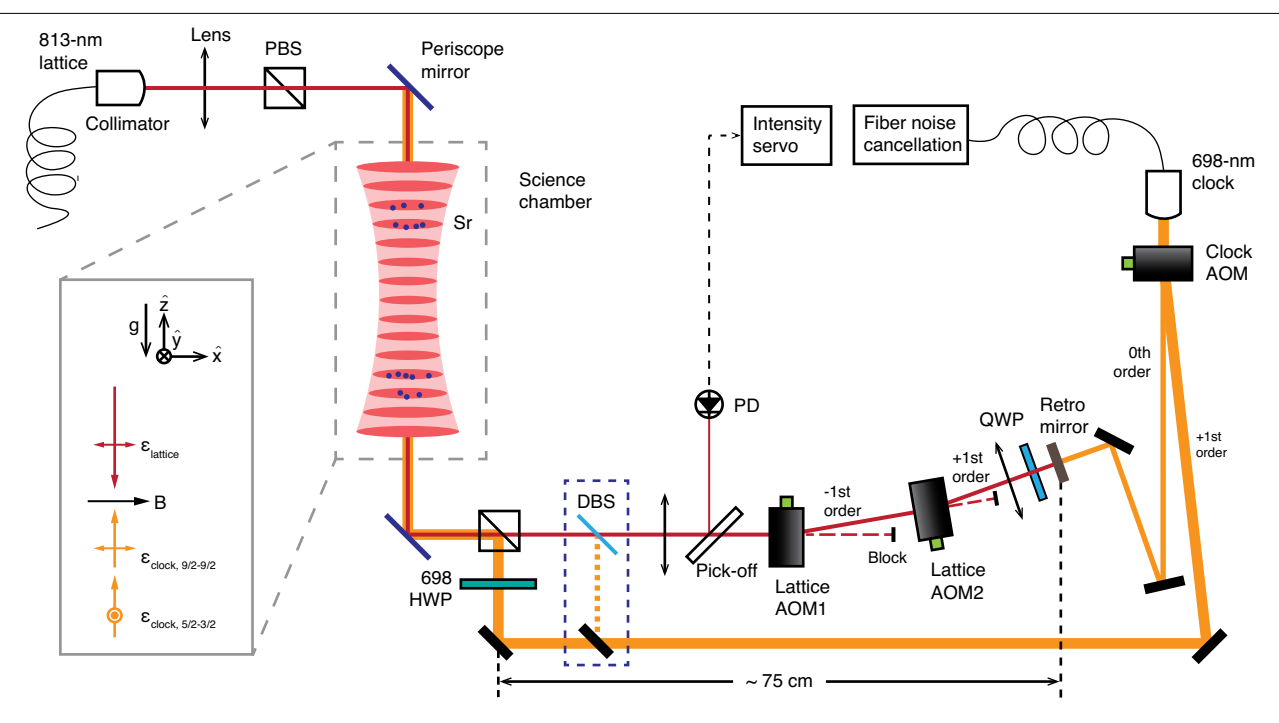
Additional information

Supplementary information The online version contains supplementary material available at https://doi.org/10.1038/s41586-021-04344-v.

 $\textbf{Correspondence and requests for materials} \ \text{should be addressed to Shimon Kolkowitz}.$

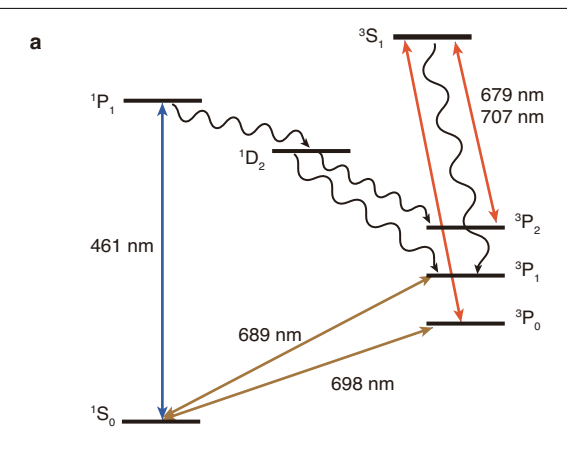
Peer review information *Nature* thanks the anonymous reviewers who contributed to the peer review of this paper. Peer reviewer reports are available.

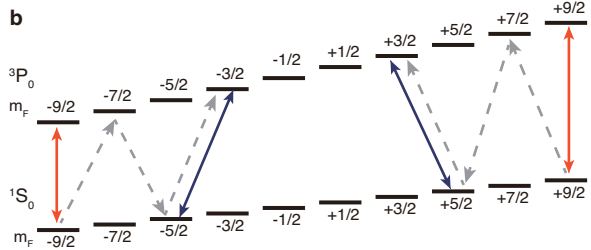
 $\textbf{Reprints and permissions in formation} \ is \ available \ at \ http://www.nature.com/reprints.$



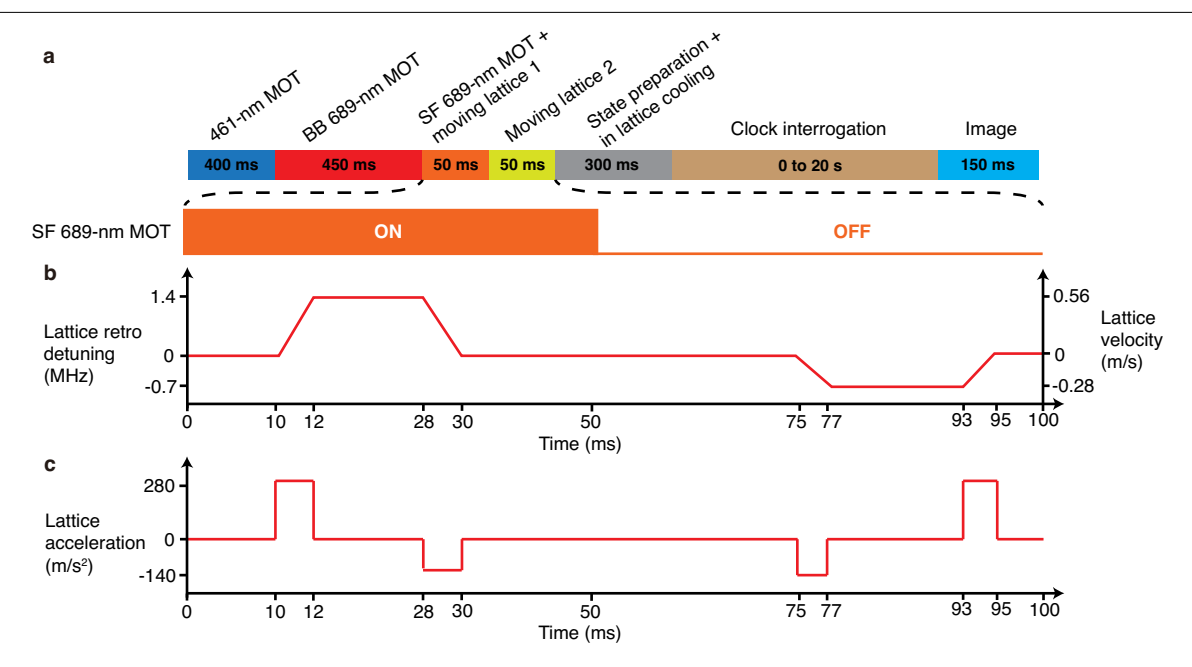
Extended Data Fig. 1 | **Lattice and clock path.** Schematic diagram showing the lattice and clock beam paths for the interrogation the $|^1S_0, m_F = \pm 5/2\rangle \leftrightarrow |^3P_0, m_F = \pm 3/2\rangle \sigma$ -transition. To interrogate the $|^1S_0, m_F = \pm 9/2\rangle \leftrightarrow |^3P_0, m_F = \pm 9/2\rangle$ -transition, the first order diffraction clock beam is overlapped with the lattice by first using a long-pass dichroic beam splitter and subsequently transmitting through the polarized beam splitter,

shown in the dashed blue box. The inset shows the corresponding orientations of the bias magnetic field (B) and the lattice and clock polarizations (ϵ). Abbreviations: PBS, polarized beam-splitter; DBS, dichroic beam-splitter; AOM, acousto-optic-modulator; PD, photo-diode; HWP, half-waveplate; QWP, quarter-waveplate.



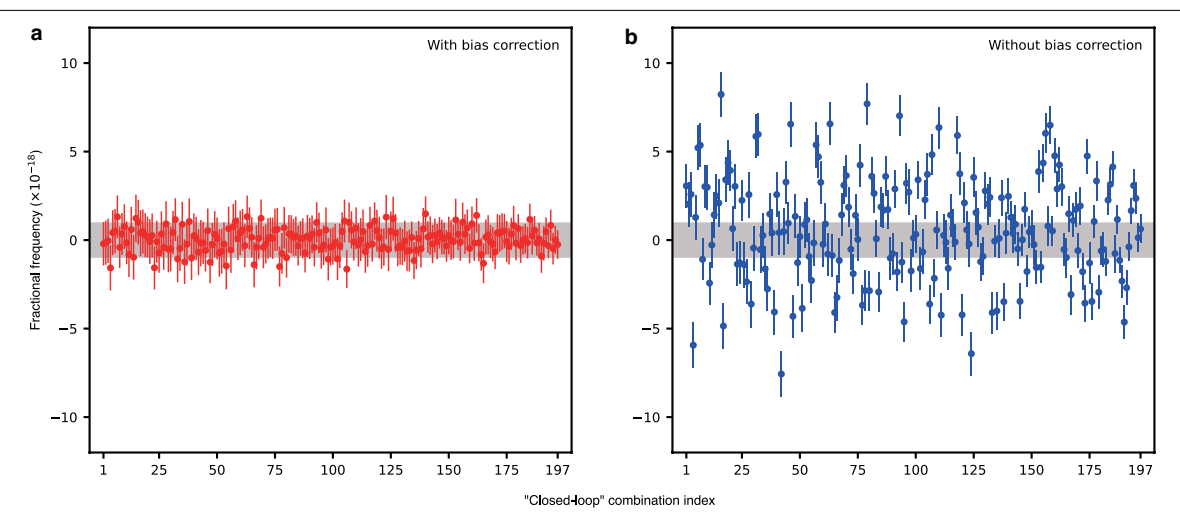


Extended Data Fig. 2 | **Energy levels diagram. a**, Energy level diagram for strontium. The double-arrow lines correspond to the relevant transitions, including the 461-nm ${}^1S_0 \leftrightarrow {}^1P_1$ transition for the first-stage MOT and imaging, the 689-nm ${}^1S_0 \leftrightarrow {}^3P_1$ transition for narrow-linewidth MOT, spin-polarization and in-lattice-cooling, the 679-nm ${}^3P_0 \leftrightarrow {}^3S_1$ and 707-nm ${}^3P_2 \leftrightarrow {}^3S_1$ transitions for repumping, and the 698-nm ${}^1S_0 \leftrightarrow {}^3P_0$ transition for clock interrogation. The wavy lines correspond to spontaneous emission. **b**, Hyperfine clock states. Red double arrows represent clock interrogation of the ${}^1S_0, m_F = \pm 9/2 \lor \leftrightarrow {}^3P_0, m_F = \pm 9/2 \lor \leftrightarrow {}^3P_0, m_F = \pm 3/2 \lor \leftrightarrow {}^3P_0, m_F \to {}^3P_0, m_F$

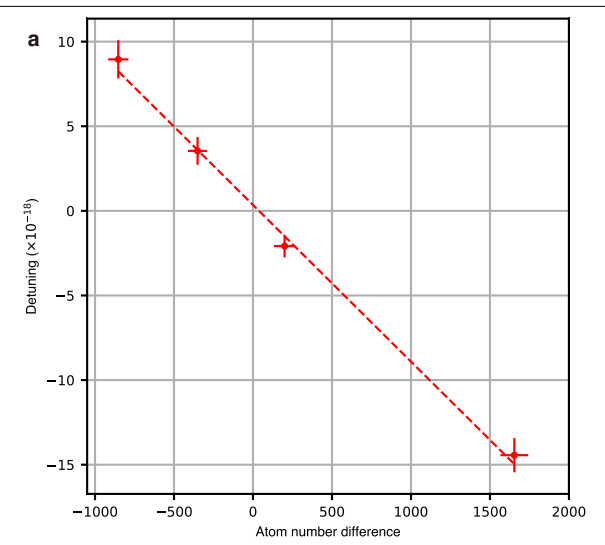


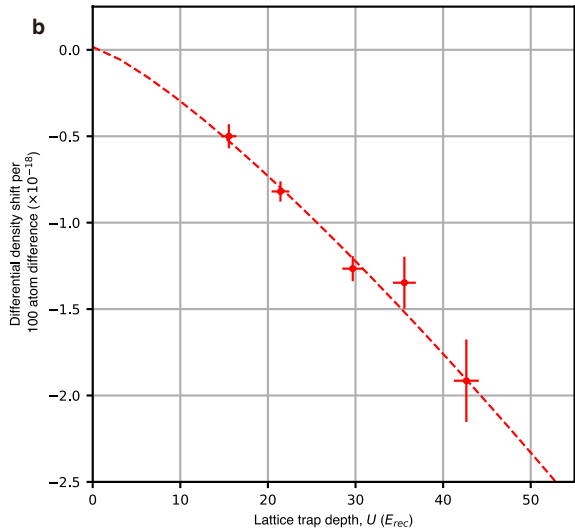
 $\label{lem:extended} \textbf{Extended Data Fig. 3} | \textbf{Timing diagram. a}, \textbf{Typical timing diagram for a} \\ \textbf{Ramsey spectroscopy sequence, in which laser cooling, state preparation and camera imaging contribute to about 1.6 s dead time, with clock interrogation} \\$

time ranging from 10 ms to 20 s. **b, c**. The corresponding lattice retro detuning, lattice velocity and lattice acceleration for loading two ensembles at 1 cm separation.



 $\textbf{Extended Data Fig. 4} \ | \ \textbf{Comparison of bias correction. a, b}, \ \textbf{Comparison of 'closed-loop' analysis with (a)} \ \text{ and without (b)} \ \text{bias correction. 197 unique} \ \text{'closed-loop' combinations are shown, with each datum corresponds to the sum frequency within each loop. Shaded area represents a window of 1 \times 10^{-18}.$





Extended Data Fig. 5 | **Differential density shift. a**, Measured differential density shift as a function of atom number difference between two symmetrically prepared ensembles at 1 cm separation. The data is taken at $20E_{\rm rec}$ lattice trap depth with 6 s interrogation time. Dashed line is the linear

fitting, in which the slope is extracted as $-8.5(6) \times 10^{-19}$ shift per 100 atom number difference. **b**, Scaling of differential density shift per 100 atom number difference between ensemble pairs with lattice trap depth U. The dashed line is a fit to the expected $\alpha U^{5/4} + \beta$ scaling 20 , where α and β are fit parameters.

Extended Data Table 1 | Measured coherence times

	1/e decay time	Fitting
Ramsey with one ensemble	96(24) ms	Gaussian
Ramsey with two ensembles, $9/2 \leftrightarrow 9/2$	6(1) s	Gaussian
"Spin-echo" with two ensembles, $9/2 \leftrightarrow 9/2$	24(5) s	exponential
Ramsey with two ensembles, $5/2 \leftrightarrow 3/2$	26(2) s	exponential

Uncertainties are quoted as 1σ standard deviation.

Extended Data Table 2 | Differential frequencies from 6 ensemble measurement

<u></u>	1	2	3	4	5	6
1	_	_	_	_	_	_
2	61.17(16)	_	_	_	_	_
3	125.74(19)	64.67(17)	_	_	_	_
4	196.67(15)	135.57(15)	70.65(18)	_	_	_
5	274.83(15)	213.69(22)	148.88(23)	78.15(20)	_	_
6	360.19(15)	299.02(20)	233.96(23)	163.66(16)	85.43(25)	_

Differential frequencies are defined as $\delta f_{ji} = -\delta f_{ij} = f_j - f_{i}$, where i, j are indices of ensembles. All units are in mHz, with errors of 1σ standard deviation.